Icarus **142**, 402–413 (1999)
Article ID icar.1999.6192, available online at http://www.idealibrary.com on IDEAL®

Lunar Cold Traps: Effects of Double Shielding

V. Carruba

Cornell University, 516, Space Sciences Building, Ithaca, New York 14850

and

A. Coradini

Consiglio Nazionale delle Ricerche, Area di Ricerca di Roma Tor Vergata, Istituto di Astrofisica Spaziale, Via Fosso del Cavaliere, 00133 Rome, Italy
E-mail: Coradini@saturn.ias.rm.cnr.it

Received September 8, 1997; revised June 22, 1999

This paper deals with the problem of water permanence on the surface of the Moon. Possible zones where water ice can survive are called cold traps (K. Watson, B. C. Murray, and H. Brown 1961, *J. Geophys. Res*. 66, 3033–3045). These are zones of the Moon permanently obscured where the temperatures are low enough to preserve ice for billions of years. In this work we developed a model for the topographic temperatures of complex craters whose shape was approximated by a capsized frustum of a circular right cone. Double-shaded areas were simulated by embedding a small hemispherical crater in the shadowed part of the previous one. Their temperatures were calculated using the R. R. Hodges, Jr. (1980, *Proc. Lunar Planet. Sci. Conf. 11th*, 2463–2477) model. First we verified that our results were in agreement with those of previous models. Our results confirm those obtained by J. R. Salvail and F. P. Fanale (1994, *Icarus* 111, 441–445), and in agreement with Hodges (1980), we found that the lowest temperatures are reached by Tycho-like craters that are the larger and shallower among the examined cases. When small craters are embedded in the shaded area of larger ones, their temperatures are low enough to preserve other volatiles like CO_2 (Hodges 1980). In particular, if we consider double-shaded areas in Biot-like craters, the temperatures are lower than 103 K in a shell of almost 20° around the poles, thus allowing the preservation of ices. For geometrical reasons a hemispherical crater embedded in the bottom of a Biot-like crater cold remain in the shadowed area for latitude values lower than those reached by an analogous crater embedded in Sosigene or Tycho-like craters. Therefore the latitudinal radius of polar frost caps could be greater than that predicted by previous models that did not consider double-shaded areas. However, double shielding occurs in only a fraction of the secondary craters; therefore, in this case eventual deposits of ice would be of smaller dimensions compared with the case of primary shielding. Analysis of the Clementine radar data (S. Nozette, C. L. Lichtenberg, P. Spudis, R. Bonner, W. Ort, E. Malaret, M. Robinson, and E. M. Shoemaker 1996, *Science* 274, 5292–5300) and the Lunar Prospector neutron spectrometer data seems to be consistent with the presence of water ice in very low concentrations across a significant number of craters, thus confirming the old hypothesis of Watson *et al*. (1961).

Key Words: **Moon; Moon surface; ices.**

1. INTRODUCTION

The possibility that water ice may exist in permanently shadowed regions in circumpolar craters on the Moon has been investigated and debated since the Watson *et al*. (1961) work. Arnold (1979) investigated the stability of trapping mechanisms for water ice in polar regions of the Moon. Hodges (1980) obtained estimates of equilibrium surface temperatures in permanently shadowed regions on the Moon. Lanzerotti *et al*. (1981) suggested that sputtering by solar wind ions would remove ice as fast as it is deposited in the cold traps. However, Arnold (1990) pointed out that shadowed regions are normally shielded from the solar wind, which would minimize the effect of sputtering. Recently, radar observations of Mercury (Slade *et al*. 1992, Harmon and Slade 1992) indicated the presence of water ice in the vicinity of the poles. A $4^\circ \times 8^\circ$ oblong region incorporating the North Pole and the region inside Chao Meng Fu crater near the South Pole was found to exhibit properties suggestive of water ice. In response to this discovery. Paige *et al*. (1992) developed a thermal model to investigate the thermal stability of water ice at the poles of Mercury. They found that the temperatures of flat, low-reflectivity surfaces at Mercury's poles is not expected to exceed 167 K and that temperatures in permanently shadowed regions of larger impact craters could be as low as 60 K. Ingersoll *et al*. (1992) investigated the stability of polar frosts in spherical bowl-shaped craters on the Moon, Mercury, and Mars. They presented analytical solutions for the effective albedo, the effective emissivity, and the radiative equilibrium temperatures in the shadowed portions of spherical, bowl-shaped craters.

In 1994 Salvail and Fanale published the results of a model of thermal equilibrium in craters of the Moon and Mercury. Their model, when assigned a topography and a grid of surface elements, calculates at each grid point the irradiation caused

0019-1035/99 $30.00

by the direct insulation of the considered element and by the emitted and reflected radiation from other elements. In this work the shadow profile in the crater, the partial obscuration of the solar disk near the poles, and the diurnal, orbital, and seasonal variation cycles were taken into account (Salvail and Fanale 1994). The temperatures are computed on the surface grid as a function of the local topography and for the entire astronomical cycle, including the effects of the direct and indirect irradiation, infrared radiation, heat conduction, and internal heating. The vapor fluxes and the recession times of the ice are computed as a function of the ice depth on the surface grid.

It is the most complete numerical model on the thermal equilibrium in the cold traps ever published. Here we present a new analytical model that permits remarkable flexibility. The two models are so complementary. With the Salvail and Fanale approach one can make a large-scale estimation of the zone where the possibility of finding ice is higher. With our model it is possible evaluate a local situation where the topography is well known.

The general topography of the Moon is known with low resolution (<1 km), especially in south pole zones, where the possibility of finding water is higher. At this scale we can apply the Salvail and Fanale model, while our model can be applied to smaller zones like those observed during the Clementine mission. In addition, in their model Salvail and Fanale did not calculate the temperatures of the double-shaded areas, which are computed in the present work.

In the next sections we show the mathematical details of our model, and we compare our results with those obtained by Hodges (1980) and Salvail and Fanale (1994). We also show the behavior of temperature as a function of colatitude e_0, for three morphological crater types and we see that, for double-shaded temperatures, the probability of finding water is unexpectedly higher in a small hemispherical crater lying in a Biot-type complex crater. However, double shielding occurs in only a fraction of the secondary craters; therefore, in this case overall amounts of ice would be smaller in quantity than the ice preserved in primary shielding.

Finally, analysis of the data from the Clementine radar experiment (Nozette *et al*. 1996) and Lunar Prospector neutron spectrometer (Feldman *et al*. 1998) seem to be consistent with the presence of water ice in very low concentrations across a significant number of craters, thus confirming the old hypothesis of Watson *et al*. (1961) and our present evaluation.

2. THE MODEL

2.1. Thermal Equilibrium in the Lunar Cold Traps

On the surface of a permanently shadowed zone the temperature is essentially determined by four factors. These are the heat flux coming from the Moon's interior ("geothermal heat"), the solar wind, reradiation from the near-illuminated zones, and lateral conduction. At equilibrium these factors are balanced by the radiation emitted to space. The source of energy present in all the traps at about the same level is the "geothermal" source. Langseth *et al*. (1976) reported a geothermal heat flux of $\sim 2 \times 10^{-6}$ W/cm^2 in the sites of Apollo 15 and 17. Further studies by Racca (1995) seem to confirm this value. A blackbody radiating this flux would have a maximum temperature of 25 K, a value that is a lower limit (T_{c0}). For such low values of T not only H_2O and CO_2 but also CO and N_2 can remain frozen. It must, however, be pointed out that this is a maximum value for T_{c0}. Variations in the thermal conductivity of the underlying rock can cause variations in the local geothermal heat flux. To consider possible anisotropies in the rock composition, as well as topography effects on the geothermal heat flux distribution, we use the Morgan and Shemansky (1991) estimation, leading to a value for T_{c0} of about 25 K.

The heat flux of solar wind is not negligible. The flux of solar wind protons is 4.3×10^8 protons cm^{-2} s^{-1}. If all the energy of this flux is available to heat the regolith (0.84 keV/proton), the power that must be dissipated is 0.58×10^{-7} W cm^{-2} (Morgan and Shemansky 1991). This heat flux may be considered an upper limit for the contribution by energetic particles (Lanzerotti *et al*. 1981). By considering only this heat, the surface temperature would be 24 K. However, solar wind does not impinge directly on most of the lunar surface not illuminated by sunlight. It generally follows the path of solar radiation, but with a small aberration due to the orbital motion of the Earth–Moon system about the Sun (Hundhausen *et al*. 1970); Formisano, private communication, 1998). For the present problem the aberration is ignored, and the solar wind and radiation fluxes have been linearly combined.

However, when the Moon crosses the Earth's magnetotail or its magnetosheet, the flux of ions (predominantly hydrogen) is of the order of 10^5 to 10^8 particles cm^{-2} s^{-1}, with a flow dispersion of about 50° full angle (Hardy *et al.* 1975). Arnold (1979) pointed out that such a flux can potentially reach all regions of any lunar cold trap during the few days a month of lunar traversal of the magnetotail. He took as an average exposure $\simeq 10^6$ ions cm^{-2} s^{-1}, comparable to the estimate for the corotating interplanetary events (Lanzerotti 1981). The effects of these external heat sources, of the interstellar Lyman-α flux (Morgan and Shemansky 1991), and of micrometeorite bombardment are discussed in Sections 4.2 and 5.

The reradiation from nearby zones is, by far, the biggest input. It reaches a maximum at the lunar noon, and, owing to the thermal inertia of the lunar surface, it is maintained for a long period. In our model we therefore use this value of T_r. It depends on the latitude and on the orientation of the reradiating surface. The temperature of illuminated zones (T_r) is given by

$$T_r = (T_{max})(\cos\lambda)^{1/4}, \quad (1)$$

where λ is the latitude of the crater and T_{max} (=396.3 K) is the temperature that, on the Moon, a surface perpendicularly exposed to the Sun will reach. The reradiating surface would be

sloped toward the cold trap area at an angle χ, which must be subtracted from the value of λ. For example, in a trap of 75° latitude exposed to a reradiating surface inclined at 10° toward the crater plane, the value of the angle to compute in the equation will be 65°; therefore,

$$T_r = (T_{max})(\cos(\lambda - \chi))^{1/4} \simeq 320\,\mathrm{K}. \quad (2)$$

It seems a quite high temperature. Mulheman (Arnold 1979) proposed 0.373 as an exponent of $\cos\lambda$ that in the previous case would give a temperature of $\simeq$290 K. We shall adopt the first equation. Our goal is to determine the maximum possible temperature of the shadowed zone of the cold traps. We should consider that a mixed deposit of volatiles and soil has a finite depth of the order of a few meters. If the temperature at the floor of this zone exceeds 200 K, sublimation reduces the deposit's dimensions. We shall try to find polar regions where the probability of finding ices is fairly high.

We consider now the reradiation input. The thermal remitted radiation and the albedo are both assumed isotropic. Therefore, the calculated temperatures are higher than the real ones, as the lunar phase function is quite pronounced. We consider blackbody emission, and we assume that the thermal emissivity, ϵ, is constant over the crater surface.[1] With these simplifications we obtain that $T_c(1)$, the temperature of a shadowed zone due to the effect of reradiation from a sunlit surface, is defined by (Arnold 1979)

$$T_c(1) = \left(\int \frac{dS}{\pi R^2} \cos\theta_r \cos\theta_c T_r^4 \right)^{1/4}. \quad (3)$$

Actually this equation accounts only for reradiation from sunlit surfaces. The infrared flux arriving on any surface element depends on the temperature of all other surface elements, illuminated or not, that are connected to it by an unobstructed line of sight. To evaluate multiple scattering effects we used an iteration process in which we first computed the temperature of the shadowed region of the crater obtained just by reradiation from sunlit surfaces [$T_c(1)$] and we then replaced this value in the integrand. We so obtain $T_c(2)$, the temperature reached by the shaded point after two scatters of the light, which is given by

$$T_c(2) = \left[\int \frac{dS}{\pi R^2} \cos\theta_r \cos\theta_c \left(T_r^4 + T_c(1)^4\right) \right]^{1/4}, \quad (4)$$

where T_r is zero for dark areas. Multiply scattered components of solar energy and of the emitted infrared energy are considered with a similar procedure. The temperature of the shaded element, T_c, is finally given by

$$T_c = \left[T_c(n)^4 + T_{c0}^4\right]^{1/4}, \quad (5)$$

where T_{c0} (=25 K) is the equivalent temperature reached by a shaded point due only to geothermal heat and solar wind flux, and $T_c(n)$ is the temperature reached by the point due to multiple scattered solar energy and emitted infrared energy.

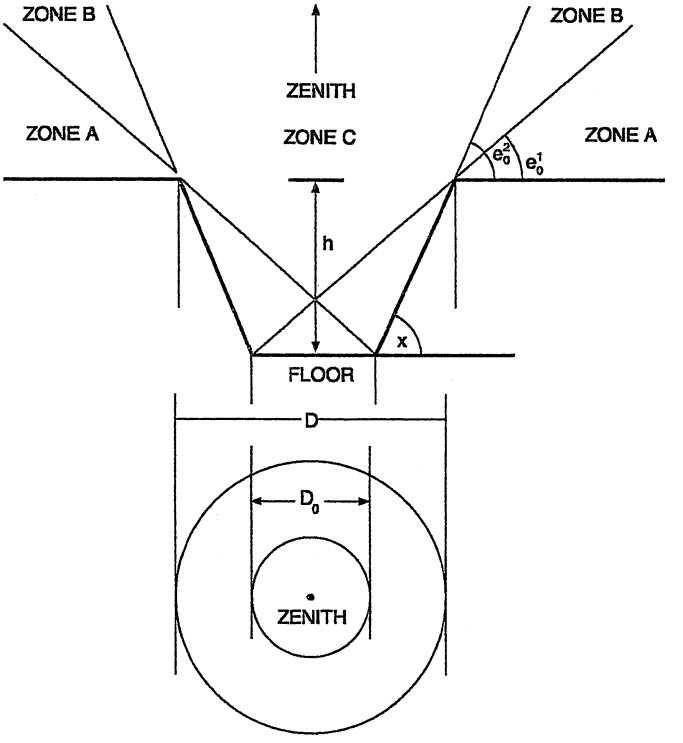

FIG. 1. Geometrical parameters of a complex crater.

The smallest input for the determination of T_c is the lateral heat flux originated by conduction from the near-illuminated zones. According to Langseth *et al.* (1976) and Brown and Matson (1987) it is possible to estimate at which scale the conduction becomes important. The result is that the heated area is about 5–10 m^2, so in a belt of such dimensions that does not receive heat from other sources the temperature will be less than 100 K. As we study only cold traps visible from Earth, whose dimensions are >1 km, this input has been neglected.

2.2. *The Adopted Geometry*

In the model presented here the geometry of the craters is approximated by considering a cone frustum whose greater base is turned to the open space (Fig. 1). The real shape of the crater walls is better described by a paraboloid, but for small values of h/D we can accept this approximation. The geometrical parameters characterizing the problem are the diameter D, the height h, the floor diameter D_0, and, more important from a physical point of view, the local azimuth of the center of the Sun e_0. The wall slope χ is defined by

$$\tan\chi = \frac{2h}{D - D_0}. \quad (6)$$

We use a cylindrical coordinate system where the origin is in the center of the crater, the y axis is oriented toward the

[1] The value of ϵ varies between 0.92 and 0.99 on the Moon (Racca 1995). The error caused by neglecting this variation is less than 0.8%.

Sun, and the z axis origin is in the cone vertex. In this way the shadow profile results are symmetric to the y axis, and it is easier to calculate the temperatures of shadowed points (we determine only temperatures of points with $x > 0$). The crater floor has $z = D_0/2 \cot \alpha$, where α is the angular half-spread of the cone. The height of the Sun on the local horizon is given by $e_0 = 90^\circ - \lambda$.

There are two limit angles, e_0^1, whose tangent is given by (Sekanina 1991),

$$\tan e_0^1 = \frac{2}{\beta(1+\gamma)},$$

where β $(=D/h)$ is the diameter-to-depth ratio, and γ $(=D/D_0)$ is the diameter-to-diameter of crater floor ratio, and e_0^2 $(=\chi)$, that define three possible situations. If e_0 is smaller than e_0^1 than the crater floor is completely obscured. If e_0 is greater than e_0^1, but smaller than e_0^2, the crater floor is only partially obscured; otherwise if $e_0 > e_0^2$ the crater floor is completely illuminated, and as it happens for values of $e_0 > 15^\circ (=\chi_{\min})$ the corresponding latitude value ($\lambda = 90^\circ - e_0 = 75^\circ$) is too high for there to be a significant probability of finding ice, so we neglect this case.

The described situation would be rigorously true if the Sun were a point source. Considering the Sun as a point involves an acceptable approximation for the Moon, where the Sun subtends an angle of 0.25°, but not in the case of Mercury where the angular diameter of the Sun is of 0.65° (Allen 1973). To obtain a model that could also be applied to Mercury we have so decided to consider this (minor) effect also for the lunar craters. As can be seen in Fig. 2 the Sun will disappear entirely from the sight of a crater point for

$$e_{0b} = e_0 + R_s,$$

where R_s is the angular radius of the Sun. We use this value to draw the shadow profile. For e_0 less than $e_{0a} = e_0 - R_s$ but greater than $e_{0b} = e_0 + R_s$, the Sun is partially eclipsed. The point illumination will not be given by $F_0 \sin e_0$ (where F_0 is the solar constant at the average distance from the Sun of the Moon) but by $F_0 f \sin e_0$, where f is the fraction of solar disk noneclipsed (for its determination see Section 3.1); the temperature of this point will be reduced by a factor $f^{0.25}$. In the next section we define the shadow profile.

2.3. Shadow Profile

We are not interested in the noon shadows, but we want to determine the permanent shadow profile as we look for permanently obscured crater zones. They would be only a fraction of noon shadowed areas, as zones not illuminated at noon can be irradiated for lower values of the Sun's height above the horizon. To draw the permanent shadow profile, we follow a process already used by Hodges (1980). The terminator is marked out by an ellipse (defined by the intersection of a plane parallel to the Sun's direction with the cone) on the crater walls and a straight line on the crater floor, if the floor is partly illuminated.

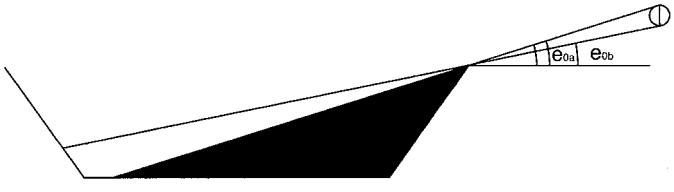

FIG. 2. Effects of the Sun's angular dimension on the shadow profile.

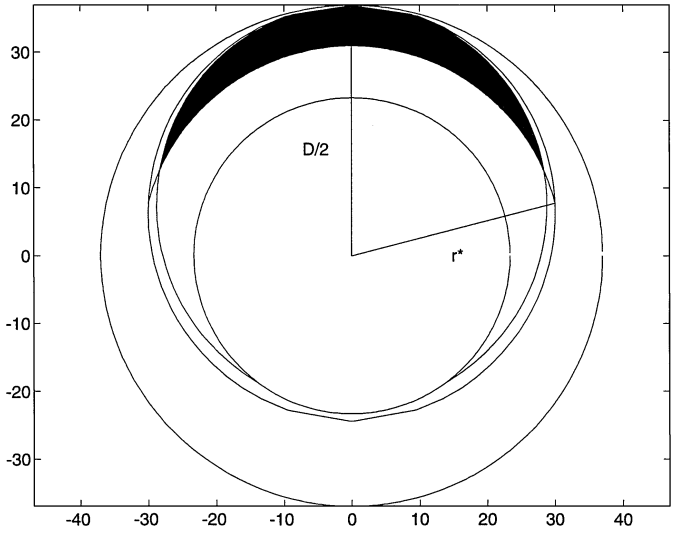

FIG. 3. Half-lit zone. The presence of the rim introduces a half-lit area (in black) in the upper part of the shadowed crater walls.

As far as the rim of the crater is concerned we used the following approach. According to Pike (1977), many craters have rims whose heights follow the expressions

$$R_e = 0.036 D_r^{1.0141} \quad (D < 17 \text{ km}), \tag{7}$$

$$R_e = 0.236 D_r^{0.0399} \quad (D > 17 \text{ km}). \tag{8}$$

The rim profile cannot be too sharp, due to erosion and bombardment by smaller projectiles, and this implies the existence of a half-lit area in the upper part of the shadowed crater walls. We consider this effect by introducing in our model a half-lit zone described as a circle of radius $D/2$, a circle of radius $r^* = D/2 - 2R_e \tan \alpha$, and the shadow profile (see Fig. 3) where the temperatures are considerably lower than in the directly illuminated zones but higher than in the shadowed area. The effect of these zones is to slightly augment the permanently shadowed area temperatures.

So, the shadow profile in our craters is divided into three zones: the illuminated zone, the zone shielded from direct solar illumination, and the transition zone where the Sun is partially eclipsed.

3. TEMPERATURE DISTRIBUTION

3.1. The Illuminated Zones

In Section 2 we formulated the expression of the temperature of surfaces directly exposed to the Sun, horizontal and inclined.

In this section we modify these equations to account for the particular geometry of the problem; we also discuss the case of points looking at a partially eclipsed Sun and we obtain their temperature. We start with the surfaces exposed to the complete solar disk. For points on the crater floor the temperature is given by Eq. (1).

The situation is more complicated for points on the crater walls. For $x = 0$ and y in the range $\frac{-D_0}{2}-\frac{-D}{2}$ (points directly exposed to the Sun which is assumed to be in the $+Y$ direction) the temperature is given by Eq. (2), while for off-center points we consider the cosine of the Sun line with respect to the surface normal. The unit vector pointing from the crater to the Sun is

$$\hat{y}\,\cos e_0 + \hat{z}\,\sin e_0.$$

The normal to the conical crater walls is

$$-\hat{x}\sin\chi\sin\theta - \hat{y}\sin\chi\cos\theta + \hat{z}\cos\chi,$$

where θ is the angle between the surface element and the direction of the Sun (measured from the $+Y$ axis) and χ is the wall slope. The dot product of these vectors gives

$$\sin e_0\cos\chi - \cos e_0\sin\chi\cos\theta$$

and, therefore:

$$T_{\rm r} = (T_{\max})(\sin e_0\cos\chi - \cos e_0\sin\chi\cos\theta)^{1/4}. \qquad (9)$$

For $\theta = \pi$ we reobtain Eq. (2). We still have to consider zones where the Sun is partially eclipsed. To calculate the insulation when the Sun is cut by the horizon, we consider a coordinate system centered in the solar disk with the z axis vertical and the horizon at $z = -h'$. In this case, according to Landau (1982), the insulation S is given by

$$S = 2F_0\int_{-h'}^{R_{\rm s}}\left(R_{\rm s}^2 - z^2\right)^{1/2}\sin(z+h')\,dz, \qquad (10)$$

where $R_{\rm s}$ is the angular radius of the Sun. Accurate determinations of this integral show that the following approximation introduces less than 0.1% error. We define the parameter

$$\mu = \arcsin\frac{h'}{R_{\rm s}}.$$

The fraction of solar disk that is visible is given by (Landau 1982)

$$f = \frac{1}{2} + \frac{1}{\pi}(\mu + \sin\mu\cos\mu), \qquad (11)$$

the insulation results being

$$S = f F_0\cos\lambda. \qquad (12)$$

We estimate h' from the projection of the solar disk on the crater surface.

3.2. The Shadowed Zones

We recall Eq. (3), where dS in this case is the surface element of the cone, i.e.,

$$dS = \frac{r}{\sin\alpha}d\theta\,dr. \qquad (13)$$

We only consider the integral which we call I ($T_{\rm c} = I^{1/4}$). We first treat the contributions that the illuminated walls make to the shadowed zones of the crater floor for the case of a floor partially obscured ($e_{0\rm b}^1 < e_{0\rm b} < e_{0\rm b}^2$). In this case $T_{\rm r}$ is given by Eq. (10). Observing (see Fig. 4) that $\theta_{\rm r} = \gamma$, and $\theta_{\rm c} = \pi/2 - (\gamma - \alpha)$, our integral becomes

$$I = \frac{1}{\pi\sin\alpha}\int_{D_0/2}^{D/2}dr\int_{-\theta(r)}^{\theta(r)}\frac{d\theta}{R^2}r(T_{\rm r}(\theta))^4\cos\gamma\sin(\gamma-\alpha).$$

$\theta(r)$ is determined by considering a system between the shadow profile and the cone equation. Applying the sine theorem to the triangle formed by the crater walls and R we obtain (see Fig. 4)

$$\frac{R}{\sin(\pi/2+\alpha)} = \frac{d}{\sin(\gamma-\alpha)},$$

where

$$d = \frac{(r - D_0/2)}{\sin\alpha},$$

and r is the cylindrical coordinate of the point where the sunlit is reflecting. Therefore,

$$\sin(\gamma-\alpha) = \frac{(r - D_0/2)\cot\alpha}{R}. \qquad (14)$$

From the sine theorem we also obtain

$$\frac{\sin(\pi/2+\alpha)}{R} = \frac{\sin(\pi/2-\gamma)}{c}.$$

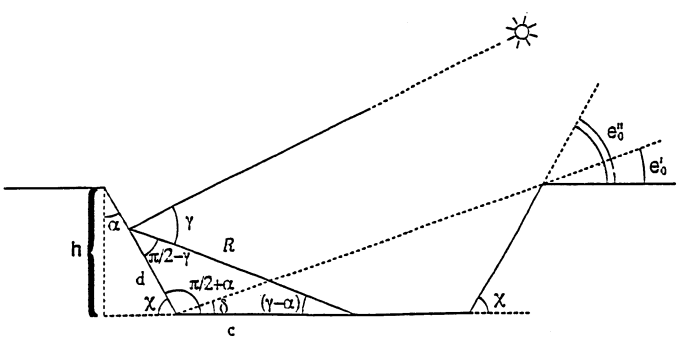

FIG. 4. Contribution from the illuminated walls to the obscured floor.

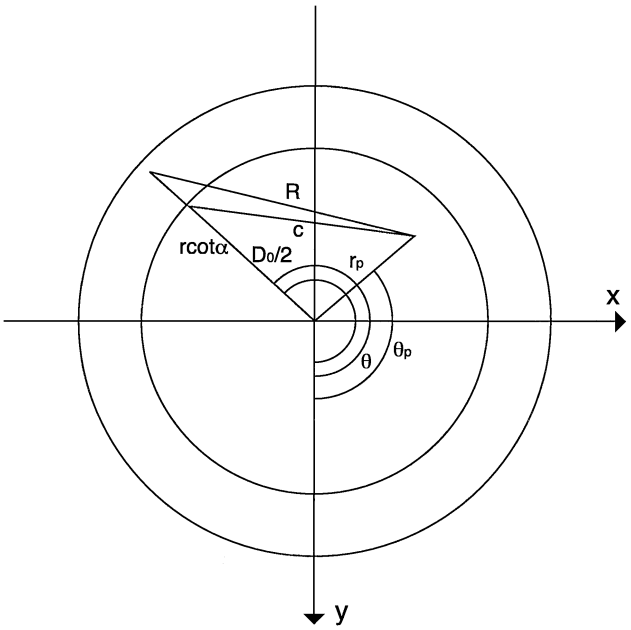

FIG. 5. Determination of c. The Sun is assumed to be in the $+Y$ direction.

Therefore,

$$\cos\gamma = \frac{c\,\cos\alpha}{R}. \tag{15}$$

Our integral I becomes

$$I = \frac{(\cot\alpha)^2}{\pi}\int_{D_0/2}^{D/2} dr \int_{-\theta(r)}^{\theta(r)} \frac{d\theta}{R^4} r\,c(T_r(\theta))^4\left(r - \frac{D_0}{2}\right). \tag{16}$$

We still have to determine the expressions for c and R. c is given by the distance, expressed in polar coordinates, between the point where we want to estimate the temperature $(r_p;\theta_p)$, and the coordinates $(D_0/2;\theta)$ (see Fig. 5). Using the law of cosines,

$$c = \left(\frac{D_0^2}{2} + r_p^2 - 2\left(\frac{D_0}{2}\right)r_p\cos(\theta-\theta_p)\right)^{0.5}. \tag{17}$$

The R^2 value is the distance between the coordinates $[r_p;\theta_p;(D_0/2)\cot\alpha)$ and the irradiating point $(r;\theta;r\cot\alpha)$, so

$$R^2 = r^2 + r_p^2 + \left(r - \frac{D_0}{2}\right)^2(\cot\alpha)^2 - 2rr_p\cos(\theta-\theta_p). \tag{18}$$

And the integrand becomes

$$f(r;\theta) = \frac{r(r-D_0/2)(T_r(\theta))^4\left((D_0/2)^2 + r_p^2 - 2(D_0/2)r_p\cos(\theta-\theta_p)\right)^{0.5}}{\left[r^2 + r_p^2 + (r-D_0/2)^2(\cot\alpha)^2 - 2rr_p\cos(\theta-\theta_p)\right]^2}. \tag{19}$$

The expression found gives the contributions of the illuminated walls to the crater floor for values of e_{0b} in the range e_{0b}^1 to e_{0b}^2. The procedures to find the same contributions for complete obscuration ($e_{0b} < e_{0b}^1$), the contributions from the illuminated floor (and from the half-lit zone) to the obscured areas, and multiple-order scatters of light are similar and, therefore, are not reported.

The previous integrals are computed numerically (we used 7200 surface elements in our calculations). We determined the temperatures of the obscured zones of a cone frustum crater when its floor is completely or partially obscured. In the next section we analyze double-shaded areas, zones of the crater also shielded from the first reflection of the solar light.

3.3. Double-Shaded Areas

The presented model assumes a flat crater floor and smooth walls. Actually the floors are usually coated by smaller craters, and the walls are often terraced [in craters with diameters larger than 150 km, there is also a central peak (Pike 1977)]. These features produce many little depressions that are permanently shadowed, not only by the direct solar irradiation, but also by the first reradiation from the illuminated zones. The easiest approximation of such double-shaded areas can be modeled by a little hemispherical crater inside the shaded zones of the crater, using a procedure already used by Hodges (1980). To compute the temperature of this crater we use the equation obtained by Hodges (1980) for the temperature of the shadowed part of a bowl-shaped crater:

$$\phi_r = \frac{\phi_s \sin e_0}{1 + (D^2/4h^2)}. \tag{20}$$

ϕ_r (constant over the entire crater surface for a bowl shaped crater) is the net reradiated infrared flux, ϕ_s is the solar constant (0.1352 W cm^{-2}), D is the crater diameter, and h is its depth. Once ϕ_r is known, we can obtain T_d (temperature of the double-shaded area) from the radiative equilibrium equation

$$T_d = \left(\frac{\phi_r}{\epsilon\sigma} + T_{c0}^4\right)^{1/4}, \tag{21}$$

where ϵ is the thermal emissivity of the surface and σ is the Stefan–Boltzmann constant. This expression is applicable to the case of solar illumination at an elevation angle of e_0. It can be adapted to a crater in a permanently shaded area by replacing $\phi_s \sin e_0$ with an effective infrared flux. This is not as simple as direct sunlight because infrared radiation arrives from all directions and it should be integrated over all illuminated surfaces. As a future development of our work, it is our intention to use Adorjan's (1970) model to account for this problem. To obtain a first approximation of the double-shaded area temperatures, we replaced $\phi_s \sin e_0$ with the effective heat flux $\epsilon\sigma T_c^4$. T_c is the temperature of the point where the bowl-shaped crater is located

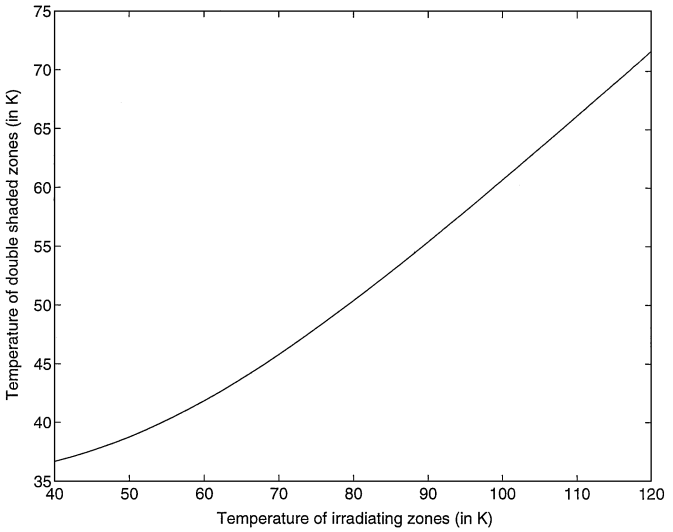

FIG. 6. Temperatures of double-shaded zones.

as computed by our model. We therefore obtain

$$T_{\rm d} = \left(\frac{T_{\rm c}^4}{1 + (D^2/4h^2)} + T_{\rm c0}^4 \right)^{1/4}. \qquad (22)$$

The temperature obtained is constant over the entire shadowed surface of the crater. It must be pointed out that double shielding occurs only in areas of a secondary crater that receive no primary infrared radiation over the entire lunar day, i.e., only in areas having no direct line of sight to the rim of the host crater. Moreover, for geometrical reasons this area decreases with increasing distance from the center of the host crater and with increasing diameter-to-depth ratio (i.e., with age) of the secondary crater.

Our calculations show (see Fig. 6) that the temperatures range from a minimum of 36 K, for $T_{\rm r} = 40$ K, to a maximum of 71 K, for $T_{\rm r} = 120$ K, temperatures low enough to preserve not only H_2O but also other volatiles like CO_2 and argon (see also Hodges 1980).

4. RESULTS

4.1. Comparison with Previous Models' Results

In this section some of the results obtained by applying our model are summarized and comparisons with similar data obtained by Hodges (1980) and by Salvail and Fanale (1994) are reported. First we show them by adopting the same geometrical parameters used by Hodges (see Table I). In Figs. 7–9 we respectively give the Hodges' results at latitudes of 85° and 80° and ours.[2] We assume that the maximum temperature occurs everywhere in permanent shadow at local noon, so our calculations do not include local time.

TABLE I
Classification and Characteristics of Flat-Floored Craters

Crater type	Diameter (km)	Diameter/depth	Walls slope (degree)
BIO(Biot)	∼14–30	5.5	22°–26°
SOS(Sosigene)	5–30	8–10	20°–26°
TYC(Tycho)	30–175	10–30	13°–15°

Source. Reproduced, with permission, from Wood and Anderson (1978).

We observe a substantial agreement between the Hodges' temperatures and ours for points on the crater floor and on the walls

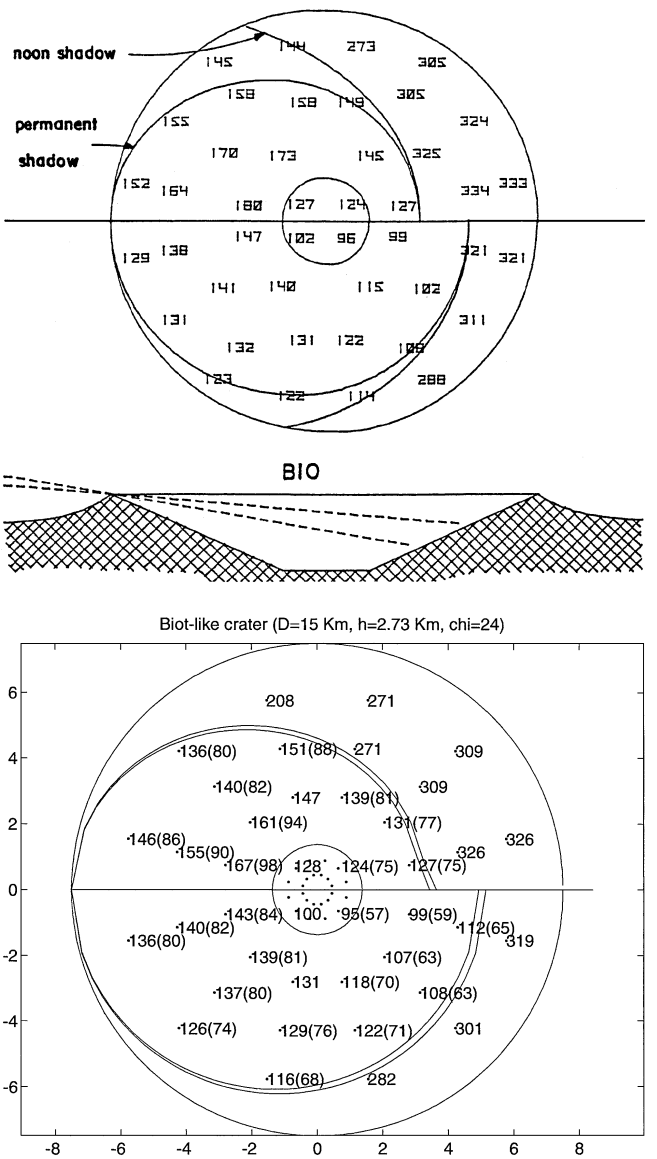

FIG. 7. Biot-like crater. (Top) Hodges' results for $e_0 = 5°$ and 10°. (Bottom) Results obtained with our model.

[2] We report only the permanent shadow profile. The data between brackets are the double-shaded temperatures; the asterisk indicates that it is a temperature reached due to the effect of partial eclipse of the Sun: the letter *h* means that the point is in the half-lit zone.

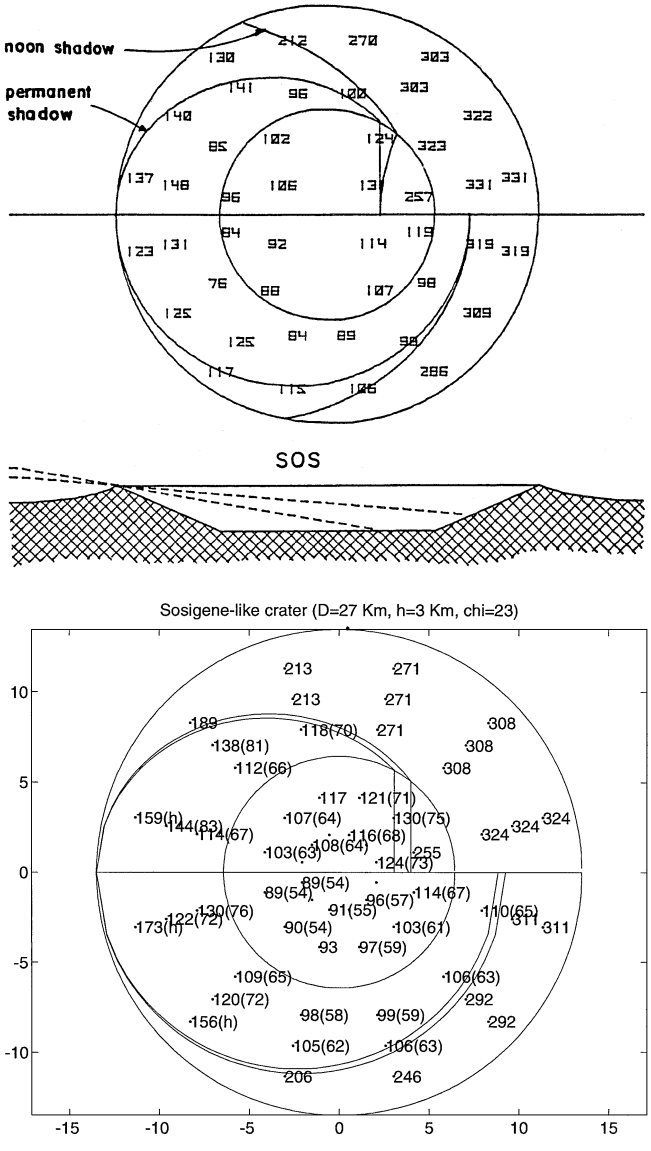

FIG. 8. Sosigene-like crater. (Top) Hodges' results for $e_0 = 5°$ and $10°$. (Bottom) Results obtained with our model.

closer to the terminator. For points on walls farther from the shadow profile, the small differences in temperature are due to the different choice of point locations and to the effects of the halflit zone (not considered in Hodges model) whose presence slightly increases the shadowed areas' temperatures.

We have then compared our data with those obtained with the Salvail and Fanale model. The authors applied their model to a real craters: the Peary crater on the Moon (D = 74 Km, h = 3.18 Km, $\chi = 13.11°$, $e_0 = 3.0°$[3]). Our results are shown in Fig. 10.

[3] The latitude of the Peary crater is 88.6°, so $e_0 = 1.4°$; we must add to this value the angle that the lunar spin axis makes with the perpendicular to the ecliptic plane and we obtain $e_0 = 3.0°$.

From a comparison of the results, we note that, considering the different locations of the points in the two figures, there is good agreement with the Salvail and Fanale results.

Ground-based measurements (Wendell and Low 1970) of high latitudes indicate a minimum temperature of the permanently shadowed regions of 84 K, a value that is in good agreement with our model result for the primary shielded zones of Tycho-like and Peary craters. Double-shaded zones do not generally cover an area large enough to be detected from Earth.

4.2. Latitudinal Radii of Polar Frost Caps

In this section we determine the limit values of e_0 which define a zone where ice can be stable for three morphological types of craters. We compute the temperatures of a point at the wall–floor contact for each type of crater and for values of e_0 that go

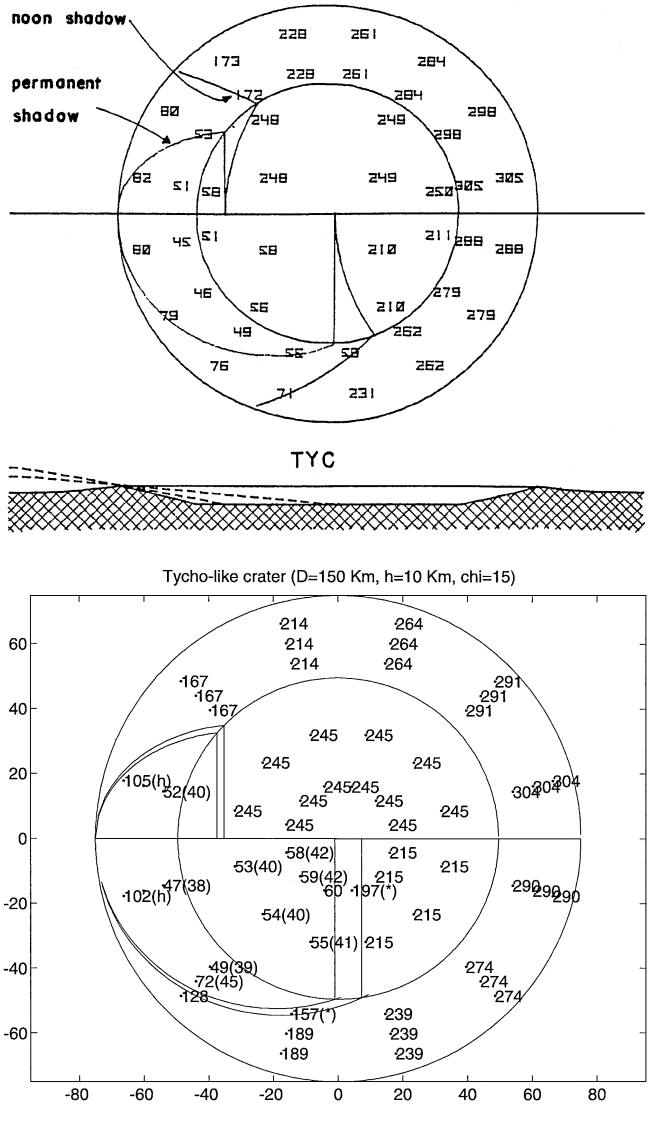

FIG. 9. Tycho-like crater. (Top) Hodges' results for $e_0 = 5°$ and $10°$. (Bottom) Results obtained with our model.

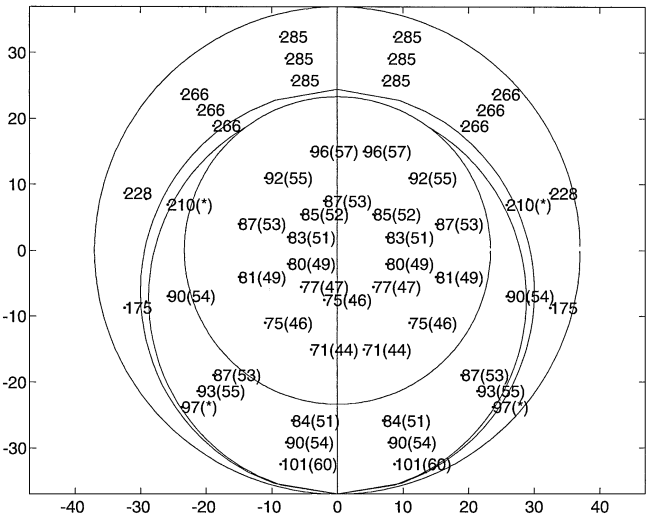

FIG. 10. Peary crater (diameter 74 km, 88.6° L): diurnal maximum temperatures ($e_0 = 3°$).

from 1.6°, the angle of inclination of the spin axis of the Moon toward the perpendicular to the ecliptic, to 40°. When the point is directly illuminated by the Sun (discontinuities in the curves). we calculate its temperature using the Ingersoll *et al*. (1992) model for bowl-shaped craters in which

$$\sigma T^4 = F_0 \sin e_0 \frac{f(1-A)}{(1-Af)}\left[1 + \frac{A(1-f)}{\epsilon}\right], \qquad (23)$$

where f is the shape factor of the hemispherical crater (given by the ratio between S_c, the crater surface area, and $4\pi r^2$; for a bowl-shaped crater whose diameter/depth ratio is 5, f is 0.1379), σ the Stephan–Boltzmann constant, F_0 the solar constant ($F_0 =$ 1370 Wm^{-2} for the Moon), A is the albedo, and ϵ is the thermal emissivity [$A = 0.068$, $\epsilon = 0.98$, average values of the lunar surface (Allen 1973)].

We then determine the value of e_0 for which the temperatures of the shadowed areas are less than or equal to 102 and 117 K. Ingersoll *et al*. (1992) estimated that the maximum sublimation rate from ice on an airless body was 0.9 cm per 10^9 years for $T = 102$ K, and 10 m per 10^9 years for $T = 117$ K. Assuming the density of ice to be 0.9 g cm^{-3} this gives a sublimation rate of 8.1×10^{-10} g/cm^2 year for $T = 102$ K and 9.0×10^{-7} g/cm^2 year for $T = 117$ K.

As we stated in Section 2.1, however, sublimation is not the dominant process of erosion. Morgan and Shemansky (1991) reexamined the erosion process of exposed deposits by considering sublimation of amorphous ice, erosion due to sputtering, and the effects of UV radiation from the interstellar hydrogen Lyman-α (HLyα). They concluded that the effects of sputtering from solar ions (which include the effects of solar wind, corotating events, magnetotail particles, and solar particle events) would destroy surface ice at the rate of 3×10^{-9} g/cm^2 year while the flux of HLyα onto the surface (permanently shadowed regions are not shielded from this flux) would cause erosion at the rate of 7×10^{-9} g/cm^2 year, making it very unlikely that a H_2O cold trap sink could develop from the continuous supply of water due to infalling meteoroids.

The effect of meteorite bombardment [which would destroy surface ice at the rate of about 1.2×10^{-9} g/cm^2 year (Arnold 1979)] combined with the two other destruction processes would destroy H_2O at a rate high enough to prevent formation of a monolayer of H_2O. Moreover, Hodges (1991) pointed out that the extreme activation energies needed to explain the adsorption of ^{40}Ar in the nighttime regolith require pristine grain surfaces not contaminated with adsorbed water. It is our opinion that eventual ice deposits on the Moon are not located in the upper 10–50 μm of soil, where most exospheric gas adsorption–desorption events occur, but are probably located more deeply, protected from sputtering and interstellar Lyman-α by a layer of regolith.

In their work Morgan and Shemansky concluded that ice deposits on the Moon can be due to impacts of comets on the lunar surface. If a fraction of the cometary material remains in the atmosphere for a time long enough to encounter the cold traps, some of the ice deposited can be covered with new regolith, a process that appears to have a depth scale of about 1 m per 500 myr (Gault *et al*. 1974), and, as only a small layer of regolith is required to reduce losses from the above reported erosion processes, burial can be an effective process to protect ice deposits from erosion.

While the mean interval between comet impacts is 13 myr and the average mass of a comet is of 7×10^{16} g (Ip and Fernandez 1988), the actual implacement history is likely to be quite uneven. A core tube driven into a permanently shadowed region would reveal, according to Morgan and Shemansky (1991), an uneven pattern of ice and regolith.

To estimate the radius of the zone where the probability of finding water is a maximum we chose a point on the crater floor whose temperature is a minimum (this happens for $r = D_0/2$, $\theta = 90°$). Our results are in Fig. 11. The limiting values of e_0 for the three morphological types of craters are computed in Table II ($e_0 = \pi/2 - \lambda$ is the colatitude, or the angle of the Sun on the horizon). We note that in the Tycho crater type the crater floor points do not reach the two limiting values of T before being directly illuminated by the Sun.

In Fig. 12 are reported the double-shaded temperatures of the three types of craters: the lowest temperatures are reached

TABLE II
Limit Values of e_0 as a Function of Temperature

	e_0 (deg)	
Crater type	$T_1 = 102$ K	$T_2 = 117$ K
BIO(Biot)	4.6	9.0
SOS(Sosigene)	7.0	12.0
TYC(Tycho)	<15	<15

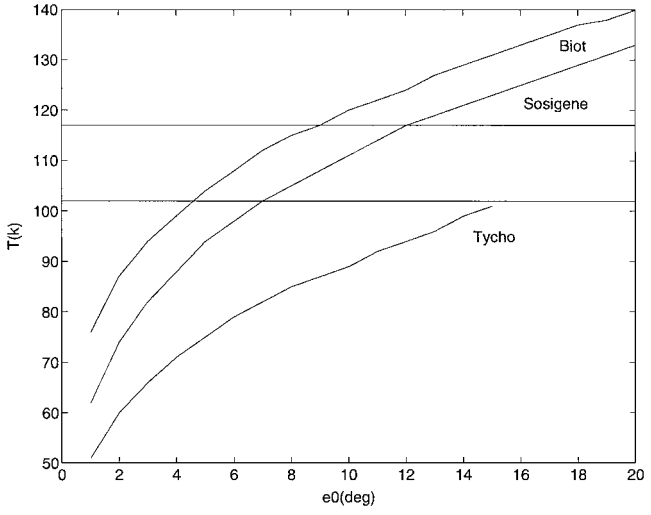

FIG. 11. Minimum temperatures of the crater floor of some complex craters as a function of the Sun's angle on the horizon. Lower temperatures are reached by craters of larger radius (Tycho-like crater).

by craters of larger radius (the discontinuities of the curve are caused by the direct illumination of the point by the Sun). We observe that a small crater placed in a crater of Biot type could preserve ice for values of e_0 greater than those placed in a Tycho-type crater, as the angle of the Sun that is necessary to directly illuminate this point is higher for this type of crater.

We argue that the zone where the probability of finding ice is maximum is about 15° around the lunar poles for craters that are shaded only once and 26° for craters that are double shaded. We must, however, point out that double shielding occurs only in a fraction of the secondary craters, as we stated in Section 3.3. Therefore in this case any deposit of ice would be smaller where compared with the case of primary shielding.

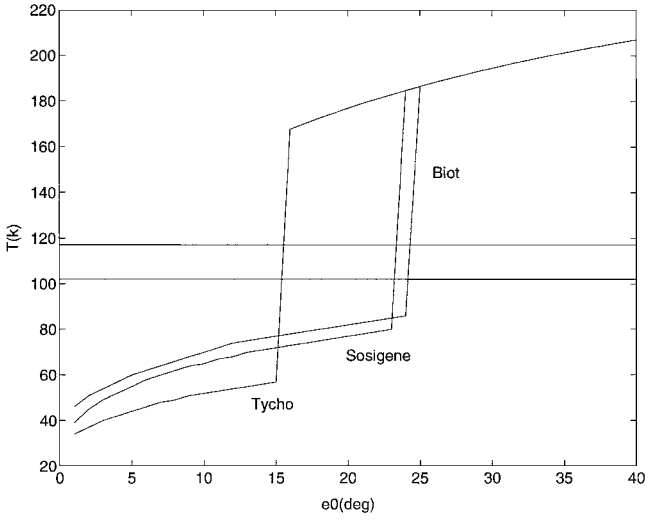

FIG. 12. Minimum double-shaded temperatures as a function of e_0 for three morphological crater types. The discontinuities of the curve are caused by the direct illumination of the point by the Sun.

The age of secondary craters is another parameter that can affect the preservation of ice deposits. Young secondary craters are more effective as cold traps as they have a smaller diameter-to-depth ratio and, therefore, the double-shaded area is larger compared with that of older eroded bowl-shaped craters. In this case the quantity of ice that can be implanted there from cometary impacts is smaller due to their young age. Older secondary craters could have preserved a larger quantity of water ice, but in this case the double-shaded area was probably reduced with increasing age.

Establishing an age–size probability distribution for viable cold traps and quantifying the effects of crater degradation on the double-shaded areas could be very important in placing some limits on ice accumulation. Estimating the effects of crater degradation on double-shaded areas would require a more detailed model of thermal equilibrium in secondary craters than what we present in this work. It is our intention in a future work to use Adorjan's (1970) model to obtain more accurate estimates of double-shaded temperatures and ice accumulation in secondary craters.

5. CONCLUSIONS AND FUTURE WORK

We developed a semianalytical model able to predict the temperatures reached inside a complex crater. The shape of the crater was approximated through a capsized frustum of a right circular cone. The presence of a smaller spherical crater embedded in the shaded part of the previous one was simulated as well. First we verified that our results are in agreement with those of previous models for the simple cases of different crater styles, without including double shading. As discussed in the previous section, our results are in good agreement with those of Fanale and Salvail (1994). It should be stressed that, in agreement with Hodges (1980), we found that the lower temperatures can be found in the dark areas of the Tycho-like craters. This is due to the lesser importance that multiple scatters of radiation have in this case.

As far as double screening is concerned, the results obtained are encouraging as we have found, in agreement with Hodges, that when small craters are embedded in the shaded area of larger craters, their volatile contents can be preserved more easily than expected. In fact, at latitudes where previous models predicted temperatures too high to preserve water ice, in some cases we found temperatures low enough to preserve even CO_2. In particular, if a small crater is present on the floor of a Biot-like crater, in a shell of almost 26° around the poles, the temperatures are lower that 103 K, thus allowing the presevation of ices. However, in this case the area that can preserve ice is smaller than in the previous case as double shielding occurs only in areas of a secondary crater that receive no primary infrared over the entire lunar day, i.e., only in areas that have no direct line of sight to the rim of the host crater. It decreases with increasing distance from the center of the host crater and with increasing diameter-to-depth ratio (i.e., with age) of the secondary crater.

The age of secondary craters is therefore a parameter that can affect the preservation of ice deposits. Young secondary craters are more effective as cold traps as they have a smaller diameter-to-depth ratio; and, therefore, the double-shaded area is larger compared with older bowl-shaped craters. In this case the quantity of ice that can be implanted there from cometary impacts is lower due to their young age. Older secondary craters could have received a larger quantity of water ice, but in this case the double-shaded area was reduced with increasing age. Establishing an age–size probability distribution for viable cold traps and quantifying the effects of crater degradation on the double-shaded area could be very important in placing some limits on ice accumulation. Estimating the effects of crater degradation on double-shaded areas would require a more detailed model of thermal equilibrium in the secondary crater than what we present here. It is our intention in a future work to use Adorjan's (1970) model to obtain more accurate estimates of double-shaded temperatures and of ice accumulation in secondary craters.

As we stated in Section 4.2, however, ice deposits are probably buried under layers of regolith, as the erosion processes caused by sputtering, Lyman-α, and meteorite bombardment can easily remove water ice from the surface (Morgan and Shemansky 1991).

Based on an earlier analysis of the Clementine radar data, Nozette *et al*. (1996) claimed detection of an enhancement in echoes with right circular polarization from a region near the south pole in a near-backscatter geometry. Such behavior would be consistent with the presence of perhaps large quantities of water ice near the pole. Simpson and Tyler (1998) were unable to reproduce that result, so the Clementine data were not conclusive for this problem. However, the more recent analysis of the Lunar Prospector neutron spectrometer data seems to be consistent with deposits of water ice in very low concentration [0.3 up to 1% mixing ratio in combination with the Moon's rocky soil (Feldman *et al*. 1998)], covered by as much as 40 cm of desiccated regolith within permanently shaded craters near both poles. A solar wind source for most of the observed excess hydrogen is considered unlikely by Feldman *et al*. because the lack of a fast-neutron signature against a surface deposit.

Lunar Prospector continued its current primary data-gathering mission at an altitude of 100 km in January 1999. At that time, the spacecraft was put into an orbit as low as 10 km so that its instruments could collect data at much higher resolution. Surface composition and structure information developed by the spacecraft's Gamma Ray Spectrometer instrument have provided new insight into the possible existence of water ice deposits on the Moon.

ACKNOWLEDGMENTS

The authors thank Teresa Capria, Gianfranco Magni, Fabrizio Capaccioni, Nives Carruba, and Priscilla Cerroni for their kind collaboration and the two unknown referees for their helpful suggestions. This work is in memory of Giovanni Gambarelli.

REFERENCES

Adorjan, A. S. 1970. Temperature distribution in shadowed lunars craters. *J. Spacecraft* **7**, 378–380.

Allen, C. W. 1973. *Astrophysical Quantities*. Univ. of London, London.

Arnold, J. R. 1979. Ice in the lunar polar region. *J. Geophys. Res*. **84**, 5659–5668.

Brown, R. H., and D. L. Matson 1987. Thermal effects of insolation propagation into the regoliths of airless bodies. *Icarus* **72**, 84–94.

Feldman, W. C., S. Maurice, A. B. Binder, B. L. Barraclo-Ugh, R. C. Elphic, and D. J. Lawrence 1998. Fluxes of fast and epithermal neutrons from Lunar Prospector: Evidence for water ice at the lunar poles. *Science* **281**, 1496–1500.

Gault, D. E., F. Hörz, D. E. Brownlee, and J. B. Hartung 1974. Mixing of the lunar regolith. *Proc. Lunar Sci. Conf. 5th*, 2365–2386.

Hardy, D. A., H. K. Hills, and J. W. Freeman 1975. A new plasma regime in the distant geomagnetic tail. *Geophys. Res. Lett*. **2**, 169–178.

Harmon, J. K., and M. A. Slade 1992. Radar mapping of Mercury: Full-disk images and polar anomalies. *Science* **258**, 640–643.

Hodges, R. R., Jr. 1973. Helium and hydrogen in the lunar atmosphere. *J. Geophys. Res*. **78**, 8055–8063.

Hodges, R. R., Jr. 1980. Lunar cold traps and their influence on argon-40. *Proc. Lunar Planet. Sci. Conf. 11th*, 2463–2477.

Hodges, R. R., Jr. 1991. Exospheric transport restriction on water ice in lunar polar traps. *Geophys. Res. Lett*. **18**, 2113–2116.

Hodges, R. R., Jr., J. H. Hoffman, and F. S. Johnson 1974. The lunar atmosphere. *Icarus* **21**, 415–426.

Hundhausen, A. J. 1968. Direct observation of solar wind-particles. *Space Sci. Rev*. **8**, 690–712.

Hundhausen, A. J., S. J. Bame, J. R. Ashbridge, and S. J. Sydoriak 1970. Solar wind proton, Vela 3 observations. *J. Geophys. Res*. **75**, 4643–4655.

Ingersoll, A. P., T. Svitek, and B. C. Murray 1992. Stability of polar frost in spherical bowl-shaped craters on the Moon, Mercury, and Mars. *Icarus* **100**, 40–47.

Ip, W. H., and J. A. Fernandez 1988. Exchange of condensed matter among the outer and terrestrial protoplanets and the effect on surface impact and atmospheric accretion. *Icarus* **74**, 47–61.

Landau, R. 1982. A comment on the insolation at Mercury. *Icarus* **52**, 202–204.

Langseth, M. G., S. J. Keihm, and K. Peters 1976. Revised lunar heat flow values. *Proc. Lunar Sci. Conf. 7th*, 3143–3156.

Lanzerotti, L. J., W. L. Brown, and R. E. Johnson 1981. Ice in the polar regions of the Moon. *J. Geophys. Res*. **86**, 3949–3950.

Lanzerotti, L. J., W. L. Brown, J. M. Poate, and W. M. Augusty-niak 1978. Low energy cosmic ray erosion of ice grains in interplanetary and interstellar media. *Nature* **272**, 431–442.

Morgan, T. H., and D. E. Shemansky 1991. Limits to the lunar atmosphere. *J. Geophys. Res*. **96**, 1351–1367.

Nozette, S., C. L. Lichtenberg, P. Spudis, R. Bonner, W. Ort, E. Malaret, M. Robinson, and E. M. Shoemaker 1996. The Clementine bistatic radar experiment. *Science* **274**, 5292–5300.

Paige, D. A., E. S. Wood, and A. R. Vasavada 1992. The thermal stability of water ice at the poles of Mercury. *Science* **258**, 643–646.

Pike, J. R. 1971. Genetic implications of the shapes of martian and lunar craters. *Icarus* **15**, 384–395.

Pike, J. R. 1977. Size-dependence in the shape of fresh impact craters on the Moon. In *Impact and Exploding Cratering* (D. J. Roddy, R. O. Pepin, and R. B. Merrill, Eds.), pp. 489–509. Pergamon, New York.

Pike, J. R. 1988. Geomorphology of impact craters on Mercury. In *Mercury* (F. Villas, C. R. Chapman, and M. S. Matthews, Eds.), pp. 165–273. Univ. of Arizona Press, Tucson.

Racca, G. D. 1995. Moon surface thermal characteristics for Moon orbiting spacecraft thermal analysis. *Proc. Lunar Planet. Sci. Conf.* **43**, 835–842.

Salvail, J. R., and F. P. Fanale 1994. Near-surface ice on Mercury and the Moon: A topographic thermal model. *Icarus* **111**, 441–455.

Sekanina, Z. 1991. Comprehensive model for the nucleus of periodic Comet Tempel 2 and its activity. *Astron. J.* **102**, 350–388.

Simpson, R. A., and L. Tyler 1998. Reanalysis of Clementine bistatic radar data from the lunar south pole. *J. Geophys. Res*., submitted.

Slade, M. A., B. J. Butler, and D. O. Muhleman 1992. Mercury radar imaging: Evidence for polar ice. *Science* **258**, 635–640.

Spudis, P. D., K. R. Stockstill, and W. J. Ockels 1995. Physical environment of the lunar south pole from Clementine data: Implications for future exploration of the Moon. *Proc. Lunar Planet. Sci. Conf. 26th*, 1339.

Thomas, G. E. 1974. Mercury: Does its atmosphere contain water? *Science* **183**, 1197–1198.

Verbiscer, A. J., and J. Veverka 1990. Scattering properties of natural snow and frost: Comparison with icy satellite photometry. *Icarus* **88**, 418–428.

Watson, K., B. C. Murray, and H. Brown 1961. The behavior of volatiles on the lunar surface. *J. Geophys. Res*. **66**, 3033–3045.

Watson, K., B. C. Murray, and H. Brown 1962. The stability of volatiles in the Solar System. *Icarus* **1**, 317–322.

Wendell, W. W., and F. J. Low 1970. Low-resolution differential drift scans of the Moon at 22 microns. *J. Geophys. Res*. **75**, 3319–3324.

Wood, C. A., and L. Anderson 1978. New morphometric data for fresh lunar craters. *Proc. Lunar Planet. Sci. Conf. 9th*, 3669–3689.

Woronow, A., R. G. Strom, and M. Gurnis 1982. Interpreting the cratering record: Mercury to Ganymede and Callisto. In *Satellites of Jupiter* (D. Morrison, Ed.), pp. 237–276. Univ. of Arizona Press, Tucson.